

Analysis of elastic α - ^{12}C scattering with machine learning in the cluster effective field theory

Myeong-Hwan Mun,¹ Jubin Park,^{2,*} Chang Ho Hyun,³ and Shung-Ichi Ando^{3,4}

¹*Department of Physics, Kyungpook National University, Daegu 41566, Korea*

²*Department of Physics and Origin of Matter and Evolution of Galaxies Institute,
Soongsil University, Seoul 06978, Korea*

³*Department of Physics Education,
Daegu University, Gyeongsan 38453, Korea*

⁴*Department of Display and Semiconductor Engineering
and Research Center for Nano-Bio Science,
Sunmoon University, Asan 41439, Korea*

(Dated: November 11, 2025)

Abstract

We analyze the elastic α - ^{12}C scattering including the contribution of resonance states below the p - ^{15}N breakup threshold energy. We use the cluster effective field theory in which scattering amplitude is expanded in terms of the effective range expansion parameters for the angular momentum states from $l = 0$ to $l = 6$. The amplitude contains 37 parameters, which are determined by fitting to 11,392 differential cross section data points of the elastic α - ^{12}C scattering. To optimize the fitting process, we implement the Differential Evolution (DE) algorithm, which performs a global search over the high-dimensional parameter space and consistently converges to the same minimum χ^2 value across independent runs, suggesting proximity to the global minimum within the explored domain. In parallel, the Markov chain Monte Carlo method is used to cross-check the DE results and to estimate the parameter uncertainties. The best fit yields $\chi^2/N \simeq 6.2$ for the elastic scattering data. Using the determined 37 parameters, we calculate the differential cross sections and the phase shifts of the elastic α - ^{12}C scattering and compare the results with experimental data and those of an R -matrix analysis. Our result of the cross section agrees with the experimental data as accurately as an R -matrix analysis. The results demonstrate that the cluster effective field theory, combined with machine learning based optimization and uncertainty quantification, provides a reliable and systematic framework for application to low-energy phenomena relevant to stellar evolution and nucleosynthesis.

*Electronic address: `honolov@ssu.ac.kr`

I. INTRODUCTION

Effective field theory (EFT) in nuclear physics theory was initiated with the purpose to describe the strong interaction between two nucleons in free space systematically and perturbatively [1, 2]. In the EFT energy and momentum in a system or process under consideration are limited to an upper limit, which roughly divides the region above which EFT breaks down. This upper scale is combined with the counting rules that determine the order of Feynman diagrams for a specific process in the power of energy or momentum divided by the upper scale, and it becomes feasible to describe two-nucleon phenomenology at low energies on a field theoretic ground [3].

Depending on the magnitude of energy and momentum under consideration, scale parameter and counting rules are adjusted to optimize the simplicity and efficiency of the theory. For instance, if one is considering processes in the big bang nucleosynthesis era, relevant energy is below 1 MeV. At this energy scale, even the pion becomes a heavy degree of freedom. Pions are integrated out, and interactions can be described in the contact form. This theory is called pionless EFT [4, 5]. It showed accurate description of two-nucleon systems [6–8] and interactions with external electromagnetic and weak probes [9–15]. The idea of pionless EFT is extended to the systematic expansion of nuclear energy density functional to describe the infinite nuclear matter and finite nuclei, and the attempt resulted in the birth of KIDS (Korea-IBS-Daegu-SKKU) density functional [16–20]. Works with KIDS functional have been showing successful applications to diverse nuclear many-body problems such as nuclear structure [21–25], lepton-nucleus scattering [26–30] and nuclear astrophysics [31–35].

Works applying the EFT and its extensions, including the KIDS functional, to astrophysical phenomena become more and more popular nowadays. In the stellar evolution and synthesis of heavy elements, the radiative capture of α particle by ^{12}C , $^{12}\text{C}(\alpha, \gamma)^{16}\text{O}$ plays an essential role. The process primarily happens in the core helium burning stage of the stellar evolution. Temperature at this stage is well below 1 MeV, a scale much smaller than the pion mass, so interactions that drive the capture process can be described in terms of the pionless theory by treating α , ^{12}C and ^{16}O as point particles. This theory is named a cluster EFT. Application of the cluster EFT to elastic α - ^{12}C scattering showed that by adjusting the effective range expansion (ERE) parameters in the theory to the phase shifts of elastic α - ^{12}C scattering, one can reproduce the experimental data accurately in the angular mo-

momentum states from $l = 0$ to $l = 6$ [36–40]. The success proves that the cluster EFT could be a candidate for a theory applicable to the study of stellar evolution and nucleosynthesis of light nuclei.

While the α - ^{12}C capture process is so important in nuclear astrophysics, there is a critical difficulty in understanding the process. The capture process happens most actively at Gamow energy $E_G \simeq 0.3$ MeV within stars. Because the Coulomb barrier is much higher than E_G , it is extremely difficult to measure the capture cross section (or equivalently S factor) at E_G experimentally. For precise understanding of stellar evolution and synthesis of elements, it is inevitable to rely on theoretical estimation of the capture cross section. However, the status of the theory is still ambiguous that recent estimations suffer from uncertainties about 20–30 %, e.g. $S_{E1}(E_G) = 80 \pm 18$ keV b by Tang *et al.* [41] and 100 ± 28 keV b by Oulebsir *et al.* [42]. To reduce the gap, a new method may have to be attempted and advanced constraints on the uncertainty are demanded.

In this work, we adopt the cluster EFT to analyze the elastic scattering of α particle and ^{12}C . Undetermined constants of the theory corresponding to ERE parameters for the angular momentum from $l = 0$ to $l = 6$ are fitted to the elastic α - ^{12}C scattering cross section data in the energy range 2.6–6.7 MeV and 32 angle values in the range 24.0–165.9° [43]. Total number of data amounts to 11,392. To handle the large number of data efficiently and to obtain optimized results for the fitted parameters, we apply two different machine learning approaches. First, we adopt the differential evolution (DE) algorithm to determine the ERE parameters of the theory. It is known that DE is a method optimized to find global minimum over a large number of parameter space. Once the parameters are determined from the DE calculation, we use the values of DE as a starting point of the Markov chain Monte Carlo (MCMC) calculation. There are two purposes to run the MCMC algorithm: the first is a cross check of the results obtained by the DE calculation, and the second is to estimate the uncertainties of the parameters. Estimation of the uncertainty is particularly important in the extrapolation of the theory to astrophysical energy scales. It is claimed that to have a quantitative description of the helium burning process, the capture cross section at E_G should be controlled with uncertainties less than 10 % [44].

As a result of the fitting with DE algorithm, we obtain $\chi^2/N \simeq 6.23$ for the $N = 11,392$ differential cross section data. Plugging the DE results of parameters in the starting values of MCMC fitting, we obtain slightly improved accuracy $\chi^2/N \simeq 6.18$. We calculate the

11,392 differential cross section points with the 37 parameters determined from the MCMC fitting and compare the results with experimental data and R -matrix calculation. Cluster EFT reproduces the experimental cross section data as accurately as the R -matrix theory¹. To further test the theory, phase shifts are calculated from $l = 0$ to $l = 6$ and the results are compared with two R -matrix calculations [43, 45]. Most of the phase shifts from $l = 0$ to $l = 4$ agree well between cluster EFT and R -matrix theory. However, for $l = 5$ and $l = 6$, results of cluster EFT are consistent with the R -matrix results in Ref. [45], but there are substantial discrepancies with Ref. [43]. Finally asymptotic normalization constants (ANCs) of ^{16}O are calculated for the 0_1^+ , 0_2^+ , 1_1^- and 3_1^- states and the result is compared with those of previous EFT in which parameters are adjusted to the phase shift data. ANCs of 0_1^+ and 1_1^- in this work are consistent with those in the previous EFT calculation. On the other hand, the value of 0_2^+ is higher in the new result, and it is suppressed significantly in the 3_1^- state.

This study establishes a new data-driven framework that integrates the cluster EFT with machine-learning-based global optimization. Unlike conventional R -matrix or manually tuned analyses, the present approach performs an automated exploration of the entire high-dimensional parameter space, thereby avoiding dependence on initial guesses and preventing the fit from being trapped in local minima. The sequential use of the DE and MCMC algorithms ensures statistically robust convergence and provides a consistent quantification of parameter correlations and uncertainties. This methodology offers a reproducible and extensible strategy for determining the effective range parameters directly from experimental data, and it lays the groundwork for reliable extrapolation of the theory to astrophysical energy scales.

The paper is organized in the following order. In Sect. II, we describe construction of the cluster EFT and how it is applied to the elastic α - ^{12}C scattering. In Sect. III, we introduce the method to apply the machine learning to the analysis of elastic α - ^{12}C scattering and present the fitting results and consequent uncertainty. In Sect. IV, as applications of the fitting result, we present the result of the calculation of differential cross sections and phase shifts in the elastic α - ^{12}C scattering, and ANCs of the bound states of ^{16}O . Section V is dedicated to the summary and concluding remarks of the work. Appendix A shows the

¹ For a visual comparison with R -matrix, see Fig. 6 and discussions of Ref. [43].

detailed relations in the transformation between laboratory frame and center-of-mass frame and Appendix B explains in detail how to fix the effective range parameters. Appendix C summarizes the numerical values of 37 effective range parameters determined from DE and MCMC calculations.

II. ELASTIC α - ^{12}C SCATTERING IN CLUSTER EFT

In this section, we review the formalism of the differential cross section, S matrices, and scattering amplitudes of elastic α - ^{12}C scattering at low energies within the framework of the cluster EFT. The differential cross section of the elastic α - ^{12}C scattering in the center-of-mass frame is given as [45]

$$\sigma(\theta) = \frac{1}{p^2} \left| -\frac{\eta}{2\sin^2\theta/2} e^{2i\sigma_0} e^{-i\eta \ln \sin^2\theta/2} + \frac{1}{2i} \sum_{l=0}^{\infty} (2l+1) e^{2i\sigma_l} (S_l - 1) P_l(\cos\theta) \right|^2, \quad (1)$$

where θ is the scattering angle, p is the magnitude of relative momentum, $p = \sqrt{2\mu E}$, where μ is the reduced mass of α and ^{12}C , and E is the energy of α - ^{12}C system in the center-of-mass frame. η is the Sommerfeld factor, $\eta = \kappa/p$: κ is the inverse of the Bohr radius, $\kappa = Z_\alpha Z_C \alpha_E \mu$. Z_α and Z_C are the numbers of protons in α and ^{12}C , and α_E is the fine structure constant, $\alpha_E = 1/137.036$. σ_l are the Coulomb phase shifts for l th partial waves,

$$e^{2i\sigma_l} = \frac{\Gamma(l+1+i\eta)}{\Gamma(l+1-i\eta)}, \quad (2)$$

where $\Gamma(z)$ is the Gamma function. S_l are the S matrices of the elastic α - ^{12}C scattering for l th partial wave states. $P_l(x)$ are the Legendre polynomial functions. The differential cross sections are measured in the laboratory frame. The formulas for the conversion of the cross section and scattering angle between the laboratory frame and the center-of-mass frame are given in Appendix A.

The S matrices of the elastic α - ^{12}C scattering for l th partial waves are given in terms of the phase shifts, δ_l , as

$$S_l = e^{2i\delta_l} = 1 + 2ip\tilde{A}_l, \quad (3)$$

where \tilde{A}_l is the scattering amplitude for l th partial waves. We now assume that the phase shifts can be decomposed, e.g., as [39, 40]

$$\delta_l = \delta_l^{(bs)} + \delta_l^{(rs1)} + \delta_l^{(rs2)} + \dots, \quad (4)$$



FIG. 1: Feynman diagrams for dressed ^{16}O propagators. A thin dashed line and a thick dashed line denote the propagation of α and ^{12}C , respectively. A thin-thick double-dashed line with or without a filled circle denotes a dressed or bare ^{16}O propagators. A shaded oval denotes the Coulomb Green's function.

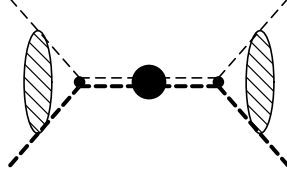


FIG. 2: Feynman diagram for the scattering amplitudes of elastic α - ^{12}C scattering in cluster EFT. A shaded oval denotes the initial or final state Coulomb wavefunction. See the caption of Fig. 1 as well.

where $\delta_l^{(bs)}$ is the phase shift generated from the scattering amplitude of a bound state of ^{16}O , and $\delta_l^{(rs1)}$ and $\delta_l^{(rs2)}$ are the phase shifts generated from the first and second resonant states of ^{16}O for the l th angular momenta. Each part of the phase shift, δ_l , is calculated by using a relation,

$$e^{2i\delta_l^{(ch)}} = 1 + 2ip\tilde{A}_l^{(ch)}, \quad (5)$$

where $(ch)annel = (bs), (rs1), (rs2), \dots$, and $\tilde{A}_l^{(ch)}$ are the scattering amplitudes, which are calculated from the effective Lagrangian in theory.

In Figs. 1 and 2, the Feynman diagrams of the dressed ^{16}O propagators for l th partial waves and elastic α - ^{12}C scattering are displayed, respectively. The propagators and vertex functions are extracted from the effective Lagrangian in Eq. (6) in Ref. [40], and the scattering amplitudes have been obtained as follows.

The scattering amplitudes for the sub-threshold bound $0_2^+, 1_1^-, 2_1^+, 3_1^-$ (l_{th}^π) states of ^{16}O were obtained as [39]

$$\tilde{A}_l^{(bs)} = \frac{C_\eta^2 W_l(p)}{K_l(p) - 2\kappa H_l(p)}, \quad (6)$$

where the functions $C_\eta^2 W_l(p)$ in the numerator of the amplitudes are calculated from the

initial and final state Coulomb wavefunctions in Fig. 2, and

$$C_\eta^2 = \frac{2\pi\eta}{\exp(2\pi\eta) - 1}, \quad (7)$$

$$W_l(p) = \left(\frac{\kappa^2}{l^2} + p^2 \right) W_{l-1}(p), \quad W_0(p) = 1. \quad (8)$$

The functions $-2\kappa H_l(p)$ in the denominator of the amplitudes are the self-energy terms calculated from the bubble diagram in Fig. 1, and we have

$$H_l(p) = W_l(p)H(\eta), \quad H(\eta) = \psi(i\eta) + \frac{1}{2i\eta} - \ln(i\eta), \quad (9)$$

where $\psi(z)$ is the digamma function. The nuclear interaction is represented in terms of the effective range parameters in the functions $K_l(p)$. Because of the modification of the counting rules [37], we include the effective range terms up to p^6 order for $l = 0, 1, 2$ and the terms up to p^8 for $l = 3$. We fix one of the effective range parameters by using a condition that the denominator of the amplitudes, i.e., the inverse of the dressed ^{16}O propagators,

$$D_l(p) = K_l(p) - 2\kappa H_l(p), \quad (10)$$

vanish at the binding energies, $E = -B_l$, where B_l are the binding energies of the sub-threshold 0_2^+ , 1_1^- , 2_1^+ , 3_1^- states of ^{16}O with respect to the α - ^{12}C breakup state. Thus, $D_l(i\gamma_l) = 0$ at $p = i\gamma_l$, where γ_l are the binding momenta, $\gamma_l = \sqrt{2\mu B_l}$, and the functions $K_l(p)$ are obtained as

$$K_l(p) = \frac{1}{2}r_l(\gamma_l^2 + p^2) + \frac{1}{4}P_l(\gamma_l^4 - p^4) + Q_l(\gamma_l^6 + p^6) + R_l(\gamma_l^8 - p^8) + 2\kappa H_l(i\gamma_l), \quad (11)$$

where $R_l = 0$ for $l = 0, 1, 2$. The effective range parameters, r_l , P_l , Q_l and R_3 are fitted to the experimental data, and one can calculate the asymptotic normalization coefficients (ANCs) of the bound states of ^{16}O with respect to the α - ^{12}C state by using the Iwinski, Rosenberg, Spruch formula [46],

$$|C_b|_l = \frac{\gamma_l^l}{l!} \Gamma(l+1 + \kappa/\gamma_l) \left(\left| \frac{dD_l(p)}{dp^2} \right|_{p^2 = -\gamma_l^2} \right)^{-1/2}. \quad (12)$$

We have 13 parameters for the sub-threshold states of ^{16}O , while we fix two of them, r_0 and r_2 , by using the binding energy of the ground 0_1^+ state of ^{16}O [47] and a value of the ANC of 2_1^+ state of ^{16}O , $|C_b|_2 = 10 \times 10^4 \text{ fm}^{-1/2}$ [48]. The detailed expressions of the modifications are presented in Appendix B.

For the scattering amplitudes for resonant states of ^{16}O , they are presented in the Breit-Wigner like expression as

$$A_l^{(rs)} = -\frac{1}{p} \frac{\frac{1}{2}\Gamma_{(li)}(E)}{E - E_{R(li)} + R_{(li)}(E) + i\frac{1}{2}\Gamma_{(li)}(E)}, \quad (13)$$

with

$$\Gamma_{(li)}(E) = \Gamma_{R(li)} \frac{p C_\eta^2 W_l(p)}{p_r C_{\eta_r}^2 W_l(p_r)}, \quad (14)$$

$$R_{(li)}(E) = a_{(li)}(E - E_{R(li)})^2 + b_{(li)}(E - E_{R(li)})^3, \quad (15)$$

where $E_{R(li)}$ and $\Gamma_{R(li)}$ are the energy and width of resonant l_{ith}^π state of ^{16}O ² and p is the relative momentum. p_r and η_r are the relative momentum and the Sommerfeld factor at $E = E_{R(li)}$, $p_r = \sqrt{2\mu E_{R(li)}}$ and $\eta_r = \kappa/p_r$. We suppressed the (li) indices on p_r and η_r for simplicity. $a_{(li)}$ and $b_{(li)}$ are the coefficients of the higher-order terms of the Taylor expansion in the denominator of the amplitudes around $E = E_{R(li)}$, which fit the shapes of the resonances.

Using the expressions of the scattering amplitudes, one has the simple and transparent expressions of the S matrices for the l th partial waves as

$$S_l = \frac{K_l(p) - 2\kappa \text{Re} H_l(p) + ip C_\eta^2 W_l(p)}{K_l(p) - 2\kappa \text{Re} H_l(p) - ip C_\eta^2 W_l(p)} \prod_i \frac{E - E_{R(li)} + R_{(li)}(E) - i\frac{1}{2}\Gamma_{(li)}(E)}{E - E_{R(li)} + R_{(li)}(E) + i\frac{1}{2}\Gamma_{(li)}(E)}. \quad (16)$$

In Appendix C, the parameters of the bound and resonant states of ^{16}O employed in the present work are summarized. Refer to Ref. [40] for details. We display three sets of fitted values of the parameters in the tables. The first set is the parameters fitted to the accurate phase shifts data reported by Tischhauser *et al.* [43]. The second one is those fitted to the differential cross section data by employing DE, and the third one is those fitted to the differential cross section data by performing MCMC.

III. RESULT OF FITTING AND QUANTIFICATION OF UNCERTAINTY

We outline the computational framework used to extract the parameters of the cluster EFT model and to quantify their uncertainties. The approach combines global optimization

² The resonant energies $E_{R(li)}$ are measured from the α - ^{12}C breakup threshold energy of ^{16}O , $E_{th} = 7.162$ MeV. The resonant energies measured from the ground state of ^{16}O are obtained by adding E_{th} , $E_x = E_{R(li)} + E_{th}$.

and sampling algorithms that are widely applied in machine learning. Parameter estimation is performed by minimizing a global chi-square over more than ten thousand elastic α - ^{12}C differential cross section data points spanning a broad range of energies and angles. Because the parameter space is high-dimensional and the objective highly non-linear, we employ global rather than local search strategies. In the first stage, DE provides a robust point estimate and ensures convergence to the minimum. This solution then serves as the starting point for a MCMC analysis, which propagates statistical and systematic uncertainties to the physical observables.

A. Differential Evolution

We fit the cluster EFT model parameters by minimizing a global chi-square over $N = 11,392$ elastic α - ^{12}C differential cross section data points covering the α -particle energies from 2.6 to 6.7 MeV and 32 laboratory angles ranging from 24.0° to 165.9° in the laboratory frame. The theoretical cross sections are calculated from the partial wave amplitudes introduced in Sect. II and transformed to the laboratory frame for direct comparison with experiment.

Before introducing the details of the fit, we note that the initial parameterization contained 41 variables in the previous works. In the $\ell = 3$ channel two coefficients are found to be redundant, while in the $\ell = 0$ and $\ell = 2$ channels the effective range terms r_0 and r_2 are constrained by the ground state 0_2^+ binding energy and the 2_1^+ ANC of ^{16}O , respectively. After applying these conditions, the number of independent parameters is reduced to 37. The fit therefore involves 37 free parameters: effective range parameters and resonance descriptors for partial waves up to $\ell = 6$. All other parameters are varied within physics-motivated bounds, with resonance widths restricted to positive values. To enforce consistency, parameter combinations leading to unphysical poles near the physical sheet are penalized and excluded from the solution.

The fit minimizes a global chi-square defined as

$$\chi^2 = \sum_{k=1}^N \left(\frac{\sigma_k^{\text{exp}} - \sigma_k^{\text{th}}(\boldsymbol{\theta})}{\Delta_k} \right)^2, \quad (17)$$

where σ_k^{exp} and σ_k^{th} are the measured and calculated cross sections, and Δ_k denotes the experimental uncertainty. $\boldsymbol{\theta}$ represents a set of effective range parameters. For data subsets

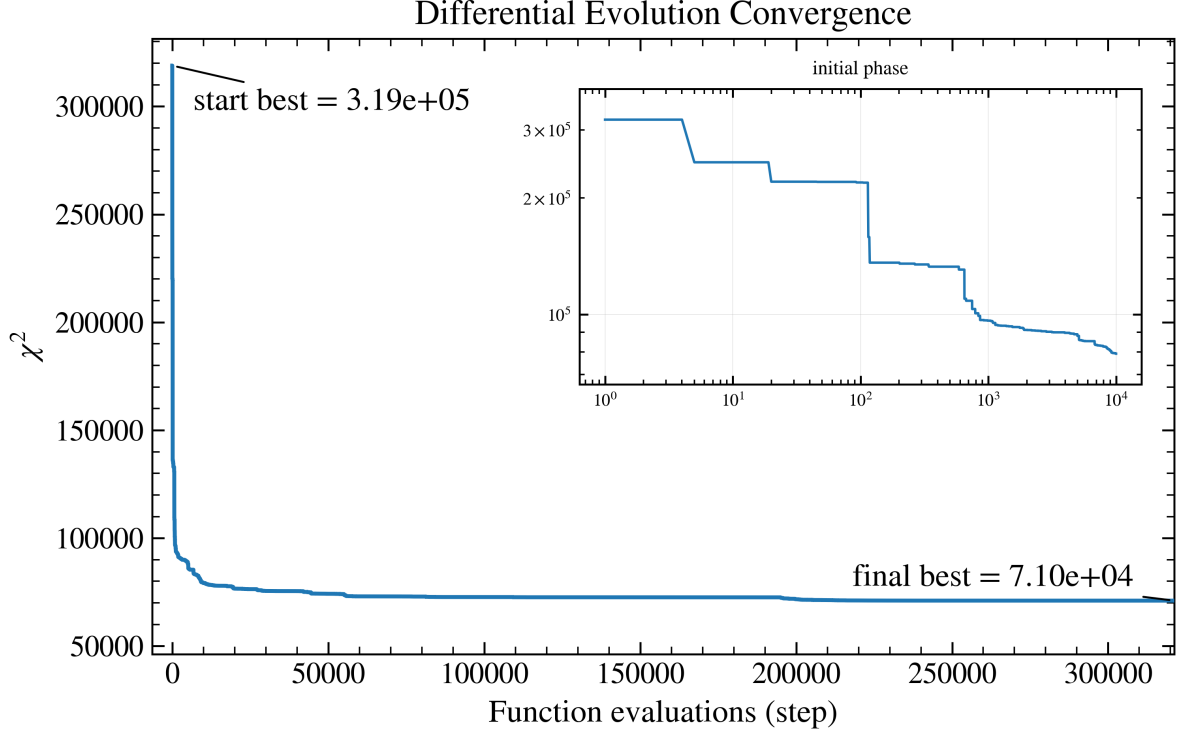


FIG. 3: Differential Evolution (DE) convergence for the 37-parameter fit. The ordinate shows the chi-square, χ^2 , constructed from the full elastic α - ^{12}C dataset ($N = 11,392$ points), while the abscissa counts objective function evaluations (“step”). The solid curve displays the running best value, $\min_{k \leq \text{step}} \chi_k^2$, which decreases monotonically from $\sim 3.19 \times 10^5$ at the start to 7.10×10^4 at the end of the run. The inset (log-log scales; steps $< 10^4$) resolves the rapid early drop and the plateau-like improvements characteristic of DE’s mutation-crossover-selection updates. Beyond this initial phase, the main panel exhibits a slow, smooth improvement and stabilization, consistent with robust global convergence.

with quoted normalization errors we introduce floating scale factors with Gaussian penalties, which absorb correlated systematics without biasing the central values.

The DE algorithm is employed to perform the global optimization. DE is a population-based, derivative-free evolutionary scheme that iteratively improves a set of candidate solutions through differential mutation, crossover, and selection. Trial vectors that yield a lower χ^2 replace their parents, driving the population toward the global minimum while maintaining sufficient diversity to prevent premature convergence. This stochastic yet sys-

tematic strategy proves well suited for the present 37-parameter fit, where the cost function exhibits multiple local minima and complex correlations among parameters. In practice we run `scipy.optimize.differential_evolution` with `strategy=rand2exp`, a population of 50 candidates in the 37 dimensional space, mutation factors $F \in [0.8, 1.9]$, and recombination rate $CR = 0.9$ [49–51]. The initial population consists of the projected reference vector θ_0 and random draws within a prior box defined by physically motivated parameter ranges. Each candidate is then projected back into the physically allowed domain, ensuring that all scattering parameters satisfy the required positivity and reality conditions imposed by the effective range formalism. The objective combines the least-squares log-likelihood (with the optional systematic floor disabled in the final runs) and a mode-selectable prior; we use the HYBRID setting, which adds soft penalties for grid positivity and mild anchors on (E_R, Γ_R) . Convergence is tracked with the running-best χ^2 trace, and the search terminates by a tolerance criterion (`tol`= 10^{-6}) or upon reaching the maximum iteration budget (`maxiter`= 10^6).

The convergence behavior of the DE fit is also summarized in Fig. 3. The plot shows the global χ^2 value evaluated over all $N = 11,392$ data points as a function of the number of function evaluations. An abrupt decrease occurs within the first $\sim 10^4$ evaluations, corresponding to the rapid elimination of high χ^2 trial vectors during the initial exploration phase. The inset, drawn on log-log scales, magnifies this region and reveals a sequence of plateau-like segments that reflects successive successful replacements of the population through mutation and crossover operations. Beyond this stage, the main panel displays a gradual and smooth improvement that stabilizes around $\chi^2 \approx 7.1 \times 10^4$, demonstrating that the algorithm has reached a well-defined global minimum without premature convergence. This behavior confirms that the adopted DE configuration efficiently explores the 37-dimensional parameter space and provides a reliable set of optimized parameters to initialize the subsequent MCMC uncertainty analysis.

Figure 4 visualizes how the DE population migrates and contracts in the 37-dimensional parameter space. Populations from generations 10^4 , 10^5 , 1.5×10^5 , 2×10^5 , 2.5×10^5 , and 3×10^5 are projected onto the first two principal components (PC1, PC2) obtained from a single principal component analysis (PCA) fitted to the union of all shown generations; points denote individual candidates, filled circles and stars mark the population centroid and best member of each snapshot, and ellipses indicate the 95% covariance regions in the

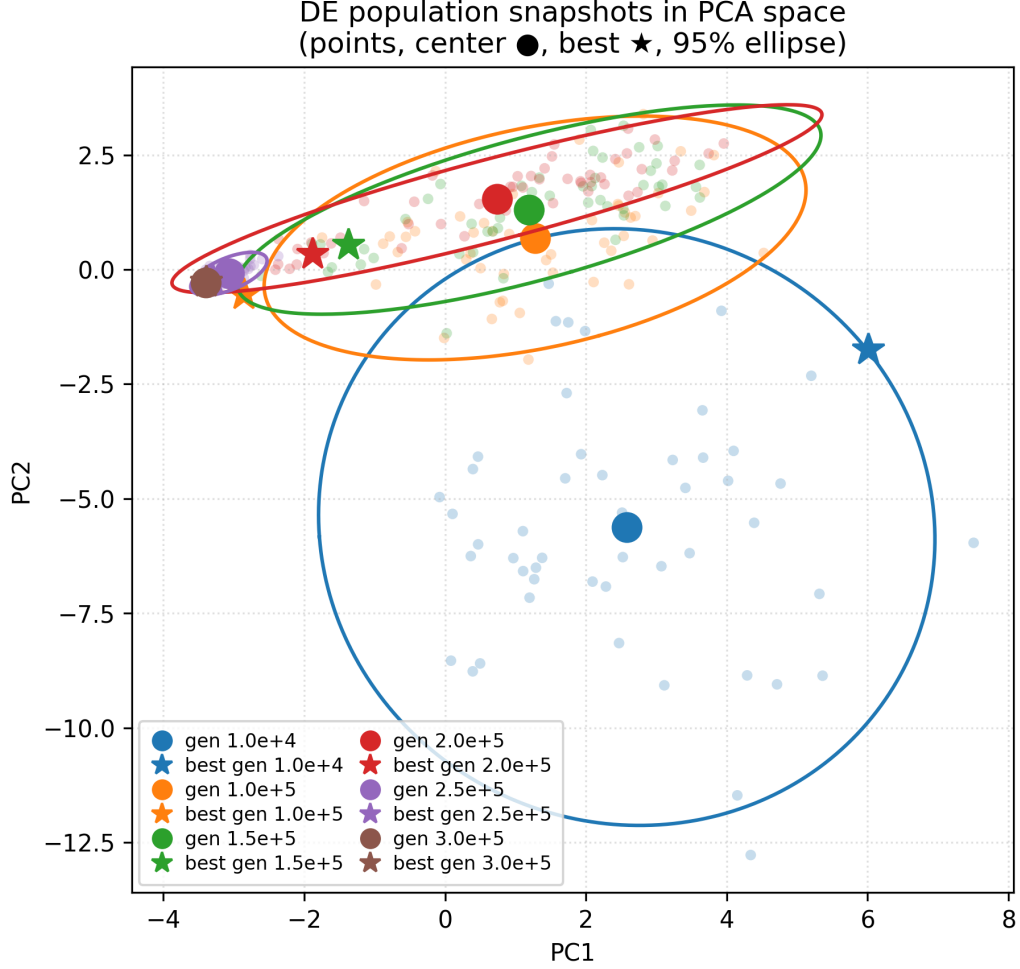


FIG. 4: Population snapshots of the DE optimization. Populations from representative generations (10^4 – 3×10^5) are projected onto the first two principal components (PC1, PC2) of a single PCA basis fitted to the combined samples. Points denote individual candidates, filled circles and stars mark the population centroids and best members, and ellipses show the 95% covariance regions. The contraction and drift of the clusters illustrate the transition from broad exploration to convergence around the global minimum. Details of the projection and interpretation are given in the text.

projected plane.³ The earliest snapshot (10^4 ; blue) is widely dispersed and appears as a large ellipse away from the later clusters, reflecting broad exploration in the projected plane. As

³ For visualization only, we compute a single PCA basis from the stacked population; PC axes are linear combinations of the original parameters and have no direct physical meaning. The ellipses are level sets of the sample covariance in the PC plane.

the run proceeds, the cloud drifts along a correlated direction (roughly aligned with PC1), the successive centroids move coherently, and the ellipses contract, with occasional mild re-expansion at intermediate snapshots as the population reorients upon entering a lower χ^2 valley; the final snapshot (3×10^5) is compact and stable. Because PCA is a linear projection of a 37-dimensional distribution, apparent sizes and orientations reflect projected covariance and can vary somewhat with the random seed and the specific snapshots shown; the qualitative pattern is robust, however: broad initial exploration, drift along a correlated valley, and eventual contraction around a single region near the optimum.

The optimized parameter vector obtained from DE serves as the initial state for the uncertainty analysis presented in Sect. III B, where MCMC propagates the resulting parameter correlations and normalization pulls to derive credible intervals for the cross sections, phase shifts, resonance parameters, and ANCs. The adopted 37-parameter configuration is validated as the minimal and physically consistent representation of the data: it simultaneously satisfies all imposed physical constraints while achieving the lowest χ^2/N among the tested configurations. Any further reduction of parameters violates at least one of the physical conditions or produces a statistically significant deterioration of the fit quality. This parametrization therefore provides a compact yet sufficient representation of the elastic α - ^{12}C scattering observables within the applicable range of the cluster EFT framework.

B. Markov Chain Monte Carlo

In Bayesian inference, as well as in general statistical modeling, the posterior probability distribution of the model parameters is often intractable to evaluate analytically. Instead of attempting to compute such complex distributions directly, the MCMC method is widely employed to approximate the posterior distribution numerically. MCMC generates correlated samples that asymptotically follow the target posterior by constructing a Markov chain whose equilibrium state represents the desired distribution. This approach enables efficient estimation of expectation values, variances, and credible intervals of the parameters, even in high-dimensional parameter spaces.

Compared with conventional deterministic optimization or least-squares fitting methods, which typically converge to a single solution or a local minimum, MCMC provides a global exploration of the entire parameter space through stochastic sampling. As a result, it allows

reliable uncertainty quantification and posterior analysis even for problems that exhibit non-linear correlations, multi-modal structures, or non-Gaussian behaviors.

In the present work, the MCMC sampling is performed using the affine-invariant ensemble sampler implemented in the `emcee` package [52]. This algorithm evolves an ensemble of multiple walkers simultaneously, enabling efficient sampling even in parameter spaces with strong anisotropy or correlations. The parameter space consists of 37 dimensions, and the ensemble comprises 200 walkers. Each walker is evolved for 120,000 steps to ensure thorough exploration of the posterior distribution, with the initial 20,000 steps discarded as burn-in to remove transient effects from initialization. A thinning factor of 10 is applied to reduce autocorrelation and enhance the statistical independence of the retained samples. Consequently, a total of approximately 2,000,000 independent samples are retained for posterior analysis. The computation is parallelized across 192 CPU cores, which significantly improves sampling efficiency and ensures robust convergence of the multidimensional posterior distribution.

The convergence of the Markov chains is primarily assessed through the integrated autocorrelation time (τ_{int}). This quantity measures the correlation length between consecutive samples, with shorter values indicating more statistically independent draws. The mean autocorrelation time over all parameters is found to be 1,434.1 steps, with a minimum of 963.7 and a maximum of 2,206.8. Given the total number of steps per walker ($N_{\text{steps}} = 120,000$), the criterion $N_{\text{steps}} \gg 50 \tau_{\text{int}}$ is well satisfied, confirming that the ensemble produces a sufficiently large number of effectively independent samples and that the Markov chains are reliably converged.

Figure 5 shows the distribution of total χ^2 values obtained from the MCMC sampling for the elastic α - ^{12}C scattering data. The χ^2 values are tightly clustered around 7.05×10^4 , with a mean of 70,489.4, a median of 70,488.8, and a minimum of 70,461.7, respectively. The narrow spread and the close agreement between the mean and the median confirm that the posterior samples are well converged, demonstrating that the model provides a stable fit to the experimental differential cross sections. The sharply peaked χ^2 distribution further demonstrates that the effective range parameters inferred from the MCMC analysis are statistically consistent and robust against sampling fluctuations.

Table I summarizes the statistical properties of χ^2/N obtained from the MCMC analysis. A total of 2,000,000 samples are used in the analysis and $N = 11,392$ represents the number

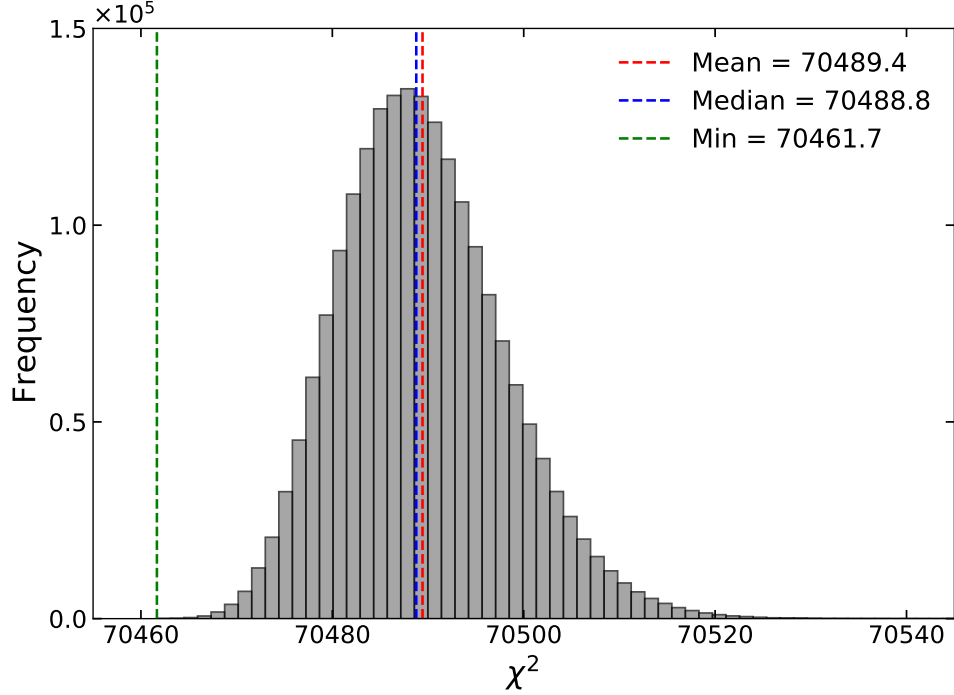


FIG. 5: Distribution of the total χ^2 values obtained from the MCMC analysis for the elastic α - ^{12}C scattering. The histogram peaks around $\chi^2 \approx 7.05 \times 10^4$, with mean = 70,489.4, median = 70,488.8, and minimum = 70,461.7, indicate excellent convergence and statistical stability of the parameter estimation.

TABLE I: Summary of χ^2/N statistics for the cross section data with the MCMC analysis. σ denotes the standard deviation, and CI implies credible interval.

Mean	σ	Median	95% (2σ) CI	Best-fit
6.1876	7.5e-04	6.1875	[6.1861, 6.1891]	6.1852

of experimental data points used in the fit. The mean value of $\chi^2/N = 6.1876$ with a very small standard deviation of 7.5×10^{-4} indicates excellent convergence of the sampling. The 95% credible interval [6.1861, 6.1891] and the best-fit value 6.1852 demonstrate that all samples are narrowly distributed, confirming the numerical stability and robustness of the MCMC results.

IV. RESULT FOR OBSERVABLES

A. Differential cross section and phase shifts with uncertainties from MCMC calculation

To comprehensively assess the consistency between the experimental data and the theoretical analysis, Fig. 6 displays the excitation curves of the elastic scattering yields for the α - ^{12}C system at eight representative laboratory angles ranging from 24.0° to 160.8° among 32 angles available from experimental data. The blue symbols correspond to the experimental yields reported by Tischhauser *et al.* [43], normalized to the yield at 58.9° to emphasize the relative energy dependence across different scattering angles, and for direct comparison with results from experiment. The red solid curves denote the theoretical predictions obtained using the EFT with effective range parameters constrained through the MCMC fitting procedure. The results are presented on a logarithmic scale to clearly illustrate the variation of the yields over several orders of magnitude within the energy range $2.6 \text{ MeV} \leq E_\alpha \leq 6.7 \text{ MeV}$. As shown in Fig. 6, the calculated excitation curves successfully reproduce both the absolute magnitude and the energy dependence of the experimental yields across the entire angular range, indicating that the extracted EFT parameters provide a coherent and quantitatively reliable description of the dynamics in the elastic α - ^{12}C scattering.

Figure 7 shows the calculated phase shifts δ_l ($l = 0-6$) for elastic α - ^{12}C scattering compared with R -matrix results [43, 45]. Blue and gray points indicate the R -matrix results, while red lines represent the result from 2,000,000 MCMC samples. The model reproduces the phase shifts consistent with R -matrix results for low angular momenta ($l = 0, 1$) and captures the main trends for intermediate values ($l = 2-4$). Phase shifts for $l = 5$ and 6 are smaller than those for $l = 0-4$, and exhibit larger uncertainties but remain consistent with R -matrix values within the MCMC prediction range. Error ranges (1σ) are denoted by green bands for each l . They are unrecognizable for $l = 0-5$, but apparent for $l = 6$. These results confirm that the MCMC-fitted model reliably describes elastic α - ^{12}C scattering across the considered angular momenta. Furthermore, the DE-MCMC approach captures both the non-resonant background and narrow resonant structures with widths above 20 keV without readjusting any parameters to specific input data, demonstrating the predictive power of this statistical inference method.

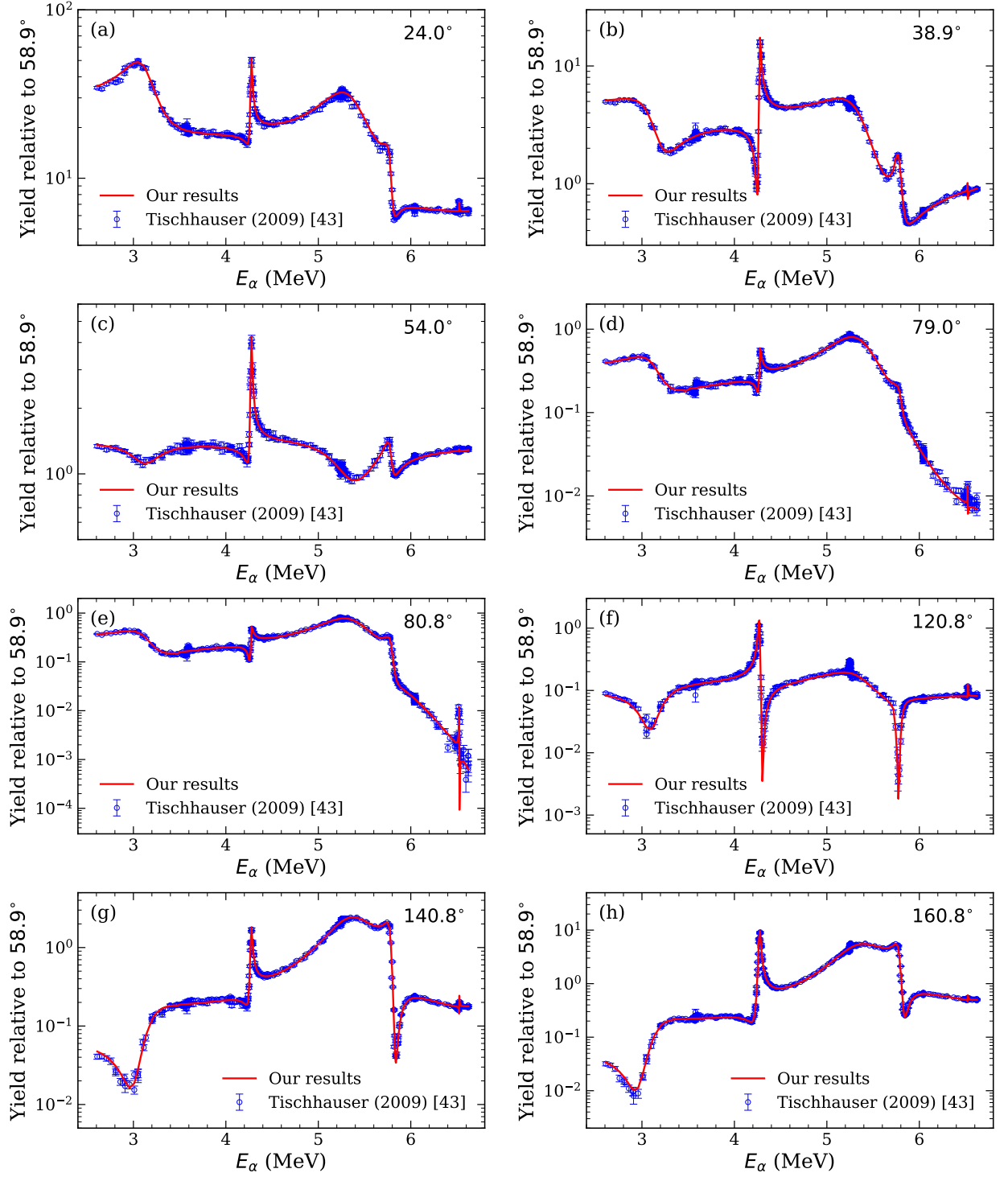


FIG. 6: Comparison between the calculated (red solid lines) and experimental (blue circle) yields as a function of the incident energy E_α for several scattering angles. The panels correspond to $\theta_{\text{lab}} = 24.0^\circ, 38.9^\circ, 54.0^\circ, 79.0^\circ, 80.8^\circ, 120.8^\circ, 140.8^\circ$, and 160.8° , respectively. The yields are normalized to those at 58.9° .

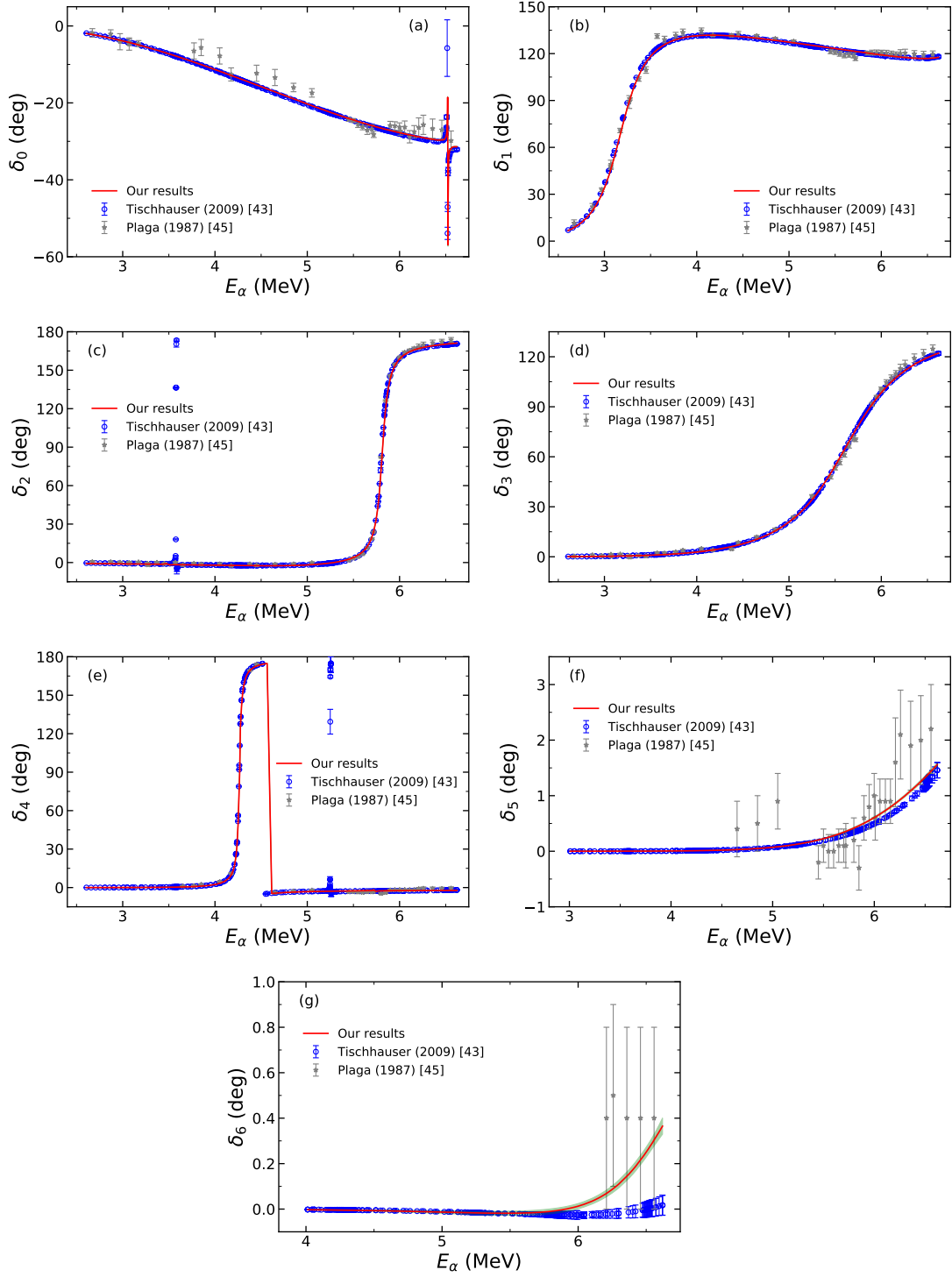


FIG. 7: Calculated phase shifts for $l = 0-6$ in elastic α - ^{12}C scattering as functions of E_α compared with R -matrix results [43, 45]. Error ranges are denoted by green bands for each l . They are unrecognizable for $l = 0-5$, but apparent for $l = 6$.

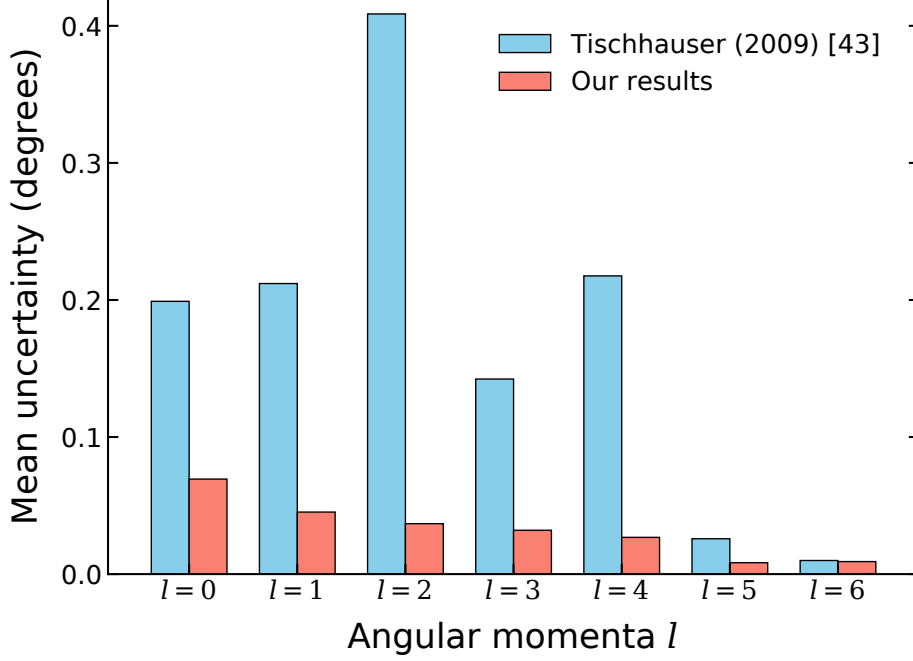


FIG. 8: Comparison of the average magnitudes of the error bars obtained in this work with those from Ref. [43]. The uncertainties from the present MCMC analysis are significantly smaller than those from the previous R -matrix evaluation.

In Fig. 8, the average magnitudes of the error bars obtained in this work are compared with those from Ref. [43]. The uncertainties extracted from the present MCMC analysis are considerably reduced compared with the previous R -matrix evaluation, demonstrating that the phase shifts are more precisely and stably constrained within the current framework. Mean uncertainty of this work is largest for $l = 0$, similar for $l = 1-4$, and $l = 5, 6$ exhibit similar smallest values. While our result shows monotonic decrease of the uncertainty with increasing l , R -matrix uncertainty exhibits strong fluctuation, ascending behavior from $l = 0$ to 3, and another low peak structure at $l = 4$ above $l = 3$. It is notable that discrepancy between R -matrix and this work is biggest at $l = 2$.

B. Resonant energies and widths, and the ANCs of bound states of ^{16}O

As seen in Fig. 7, we find the difficulty in reproducing the sharp resonant 0_3^+ , 2_2^+ , 4_2^+ states of ^{16}O in the phase shifts of R -matrix for $l = 0, 2, 4$, respectively, by using the fitted values of the parameters to the differential cross section data. The sharp resonant states

TABLE II: Fitted values of the energies and widths of the resonant 2_3^+ and 4_1^+ states of ^{16}O . The values of the second column are those in the compilation edited by Tilley, Weller, and Cheves [53]. Those in the third column are obtained by fitting to the phase shift (PS) data [40], and those in the fourth column are obtained by fitting to the differential cross section (CS) data in this work.

	TWC [53]	PS	CS
$E_{R(23)}$ (MeV)	4.358(4)	4.3536(1)	4.35902(6)
$\Gamma_{R(23)}$ (keV)	71(3)	74.5(1)	79.1(1)
$E_{R(41)}$ (MeV)	3.194(3)	3.19606(1)	3.19875(2)
$\Gamma_{R(41)}$ (keV)	26(3)	25.91(1)	27.67(6)

are clearly seen in the phase shifts reported by Tischhauser *et al.* [43] at $E_\alpha = 6.5$ MeV, 3.6 MeV, and 5.3 MeV for $l = 0, 2, 4$, respectively. The fitted values of the widths in this work turn out to be 66%, 25%, 35%, respectively, compared to the values in the previous work [40]. The energy of the resonant 4_2^+ state is also shifted significantly. The fitted values of the parameters are summarized in Appendix C. Thus, those sharp resonant states of ^{16}O are not easy to fit to the differential cross section data.

Regarding the other resonant states appearing in the data of Ref. [53], because the parameters of the resonant 1_2^- and 3_2^- states are included in the parameters of the subthreshold 1_1^- and 3_1^- states, the values of those resonant states are not fitted explicitly. In Table II, we display the fitted values of the energies and widths of the resonant 2_3^+ and 4_1^+ states of ^{16}O . The values of the second column are those in the compilation edited by Tilley, Weller, and Cheves (TWC) [53]. Those in the third and fourth columns are obtained by fitting to the phase shift data and the differential cross section data, respectively. We find a good agreement with the TWC values within the errors, except for the width of the resonant 2_3^+ state.

By using the MCMC samples of the effective range parameters, we calculate the values of the ANCs of the bound 0_1^+ , 0_2^+ , 1_1^- , 3_1^- states of ^{16}O . Because of the problem in fitting the ANC of the 2_1^+ state of ^{16}O from the elastic α - ^{12}C scattering data [48], we fixed the value of the ANC of the 2_1^+ state as $|C_b|_2 = 10 \times 10^4 \text{ fm}^{-1/2}$ in the parameter fit. See Appendix B as well.

TABLE III: The values of the ANCs of the bound 0_1^+ , 0_2^+ , 1_1^- , 3_1^- states of ^{16}O in the unit of $\text{fm}^{-1/2}$, deduced by using the effective range parameters fitted to the differential cross section data. In the previous work [54], the effective range parameters are fitted to the phase shifts data reported by Tischhauser *et al.* [43].

l_{ith}^π	Prev. work [54]	This work
0_1^+	45.5(3)	46(1)
0_2^+	621(9)	660^{+37}_{-32}
1_1^-	$1.727(3) \times 10^{14}$	$1.715(6) \times 10^{14}$
3_1^-	113(8)	75(2)

In Table III, we display the deduced values of the ANCs of the bound states of ^{16}O in the MCMC analysis with the differential cross section data, labeled by ‘This work.’ Those in ‘Prev. work’ are obtained by using the effective range parameters fitted to the phase shift data deduced in the R -matrix analysis [43]. We find that the center values of the ANC of the 0_1^+ , 0_2^+ , 1_1^- states are in good agreement within the two sigma errors, while the errors of the present work become two to four times larger than those in the previous work. Because the s -wave parts (as well as the p -wave) can contribute to the fitting of all partial waves, the errors in this work are enhanced. We also find that the center value of the ANC of the 3_1^- state becomes smaller, about 66%, compared to that in the previous work, while the error is reduced by a factor of four.

V. SUMMARY

In the present work, we attempted a new methodology for the description of elastic α - ^{12}C scattering. We adopted the cluster EFT and expanded the scattering amplitude in terms of the effective range parameters up to the angular momentum $l = 6$. Parameters were fitted to elastic α - ^{12}C cross section data in the energy range 2.6–6.7 MeV and at angles 24.0° – 165.9° including the resonance states below the p - ^{15}N breakup threshold energy. Using the DE machine learning algorithm, we could find the minimum of χ^2 in the parameter space globally. With the help of DE results, MCMC analysis was facilitated. From the analysis of correlations between parameters, we could sort out redundant parameters and as a result

identify that the optimal number of parameters is 37. Accuracy of the fitting is obtained as $\chi^2/N \simeq 6.2$ in both DE and MCMC fitting. With the MCMC method, we also estimated the uncertainty of each parameter.

Compared with conventional fitting approaches such as gradient-based searches or manually tuned R -matrix analyses, the machine-learning framework adopted here provides several practical and conceptual advantages. It performs a fully automated and global exploration of the high-dimensional parameter space, reducing the need for subjective initialization and preventing the fit from being trapped in local minima. This allows the optimization to find a physically consistent solution even when the cost surface is highly non-linear or multi-modal. The framework is also reproducible and easily extendable: once implemented, the same algorithmic pipeline can be applied to new datasets or modified models with minimal human intervention, ensuring consistency across analyses. In addition, it provides statistically rigorous uncertainty estimates through direct sampling of the posterior distribution, so that both experimental errors and model correlations are propagated in a controlled way. In this sense, the machine-learning approach does not replace traditional physics modeling but complements it, offering an objective, scalable, and data-driven means to perform global parameter optimization and uncertainty quantification within the cluster EFT framework.

To check the quality of the fitting, we calculated the differential cross sections of elastic α - ^{12}C scattering and compared the result to experimental data. Our calculation reproduces the data well, and agreement to them is as good as the R -matrix theory. We also calculated the phase shifts at angular momenta from $l = 0$ to $l = 6$ and estimated their uncertainties with the MCMC technique. We find that the phase shifts agree with those of R -matrix calculation for $l \leq 4$, but substantial enhancement occurs at high energies for $l = 5$ and 6 compared to the accurate estimate of R -matrix theory.

In the previous work [40], the phase shifts deduced in the R -matrix analysis are perfectly reproduced within the cluster EFT. However, the set of parameters that agrees with the phase shifts leads to a large χ^2 value, $\chi^2/N \simeq 20$, for the differential cross section data. Thus, we fitted the parameters of the cluster EFT directly to the differential cross section and obtained a smaller value of χ^2 , $\chi^2/N \simeq 6.2$. Because the χ^2 value of the differential cross section in the R -matrix analysis was not mentioned in Ref. [43], we have no measure to discuss which fit is better than the other. However, in the comparison of error bars in the phase shifts, average width of error bars in each angular momentum state is notably

smaller in the present work than the R -matrix results in [43]. On the other hand, we found the difficulty in reproducing the sharp resonant 0_3^+ , 2_2^+ , and 4_2^+ states of ^{16}O .

In conclusion, we have shown that the combination of effective range expansion in the cluster EFT and application of machine learning algorithms to the cross section data provide a framework accurate for the description of the elastic α - ^{12}C scattering process. With an advanced fitting scheme, uncertainty could be improved compared to precedent works. Advantage of the new method should be tested furthermore by applying it to radiative capture of α particle by ^{12}C and many other important astrophysical processes.

Acknowledgements

This work of M.-H.M. was supported by the National Research Foundation of Korea NRF grants funded by the Korean government Ministry of Science and ICT (Grants No. RS-2018-NR031074). This work of J.P. was supported by grants from the NRF of the Korean government (RS-2021-NR060129 and RS-2022-NR070836), and also by the NRF grants funded by the Korea government (MSIT, RS-2025-24533596) and the Ministry of Education (RS-2025-25400847). This work of C.H.H. and S.-I.A. was supported by the National Research Foundation grant (No. 2023R1A2C1003177). S.-I.A. was also supported by the National Research Foundation grant (No. RS-2025-16065411).

-
- [1] S. Weinberg, Phenomenological lagrangians, *Physica A* **79**, 327 (1979).
 - [2] S. Weinberg, Nuclear forces from chiral lagrangians, *Phys. Lett. B* **251**, 288 (1990).
 - [3] H.-W. Hammer, S. König, and U. van Kolck, Nuclear effective field theory: status and perspectives, *Rev. Mod. Phys.* **92**, 025004 (2020).
 - [4] J.-W. Chan, G. Rupak, and M. J. Savage, Nucleon-nucleon effective field theory without pions, *Nucl. Phys. A* **653**, 386 (1999).
 - [5] D. B. Kaplan, More effective field theory for nonrelativistic scattering, *Nucl. Phys. B* **494**, 471 (1997).
 - [6] S. Ando and C. H. Hyun, Effective field theory on the deuteron with dibaryon field, *Phys. Rev. C* **72**, 014008 (2005).

- [7] S. Ando, J. W. Shin, C. H. Hyun and S. W. Hong, Low energy proton-proton scattering in effective field theory, *Phys. Rev. C* **76**, 064001 (2007).
- [8] S. Ando, J. W. Shin, C. H. Hyun and S. W. Hong, Proton-proton fusion in pionless effective theory, *Phys. Lett. B* **668**, 187 (2008).
- [9] S. Ando, R. H. Cyburt, S. W. Hong and C. H. Hyun, Radiative neutron capture on a proton at big-bang nucleosynthesis energies, *Phys. Rev. C* **74**, 025809 (2006).
- [10] J. W. Shin, S. Ando and C. H. Hyun, Parity-violating polarization in $np \rightarrow d\gamma$ with a pionless effective field theory, *Phys. Rev. C* **81**, 055501 (2010).
- [11] S.-I. Ando, Y.-H. Song, C. H. Hyun and K. Kubodera, Spin polarization in $\gamma d \rightarrow \bar{n}p$ at low energies with a pionless effective field theory, *Phys. Rev. C* **83**, 064002 (2011).
- [12] J. W. Shin, C. H. Hyun, S.-I. Ando and S. W. Hong, Polarization of the neutron induced from hadronic weak interactions in the photo-disintegration of the deuteron, *Phys. Rev. C* **88**, 035501 (2013).
- [13] J. W. Shin and C. H. Hyun, New photodisintegration model of GEANT4 for the $d\gamma \rightarrow np$ reaction with a dibaryon effective field theory, *J. Korean Phys. Soc.* **69**, 726 (2016).
- [14] Y.-H. Song, S.-I. Ando and C. H. Hyun, Spin-polarization observables of deuteron photodisintegration at low energies in pionless effective-field theory, *Phys. Rev. C* **96**, 014001 (2017).
- [15] S.-I. Ando, Y.-H. Song and C. H. Hyun, Neutrino-Deuteron Reactions at Solar Neutrino Energies in Pionless Effective Field Theory with Dibaryon Fields, *Phys. Rev. C* **101**, 054001 (2020).
- [16] P. Papakonstantinou, T.-S. Park, Y. Lim and C. H. Hyun, Density dependence of the nuclear energy-density functional, *Phys. Rev. C* **97**, 014312 (2018).
- [17] H. Gil, P. Papakonstantinou, C. H. Hyun, T.-S. Park and Y. Oh, Nuclear energy density functional for KIDS, *Acta Phys. Polon. B* **48**, 305 (2017).
- [18] H. Gil., Y. Oh, C. H. Hyun. and P. Papakonstantinou, Skyrme-type nuclear force for the KIDS energy density functional, *New Phys.Sae Mulli* **67**, 456 (2017).
- [19] H. Gil, P. Papakonstantinou, C. H. Hyun and Y. Oh, From homogeneous matter to finite nuclei: Role of the effective mass, *Phys. Rev. C* **99**, 064319 (2019).
- [20] P. Papakonstantinou and C. H. Hyun, Energy-density modeling of strongly interacting matter: atomic nuclei and dense stars, *Symmetry* **15**, 683 (2023).
- [21] H. Gil, Y.-M. Kim, C. H. Hyun, P. Papakonstantinou and Y. Oh, Analysis of nuclear structure

- in a converging power expansion scheme Phys. Rev. C **100**, 014312 (2019)
- [22] H. Gil, N. Hinohara, C. H. Hyun and K. Yoshida, KIDS density functional for deformed nuclei: examples of the even–even Nd isotopes, J. Korean Phys. Soc. **81**, 113 (2022).
 - [23] S. Choi, E. Hiyama, C. H. Hyun and Myung-Ki Cheoun, Effects of many-body interactions in hypernuclei with Korea-IBS-Daegu-SKKU functionals, Eur.Phys. J. A **58**, 161(2022); *ibid.* **60**, 152 (erratum).
 - [24] H. Gil, N. Hinohara, C. H. Hyun and K. Yoshida, Nuclear mass table in density functional approach inspired by neutron-star observations, Phys. Rev. C **108**, 044316 (2023).
 - [25] Y. Choi, H. Gil, C. H. Hyun and C.-H. Lee, Correlation between α -decay half-lives and symmetry energy, Phys. Rev. C **111**, 034318 (2025).
 - [26] H.Gil, C. H. Hyun and K. S. Kim, Quasielastic electron scattering with the KIDS nuclear energy density functional, Phys. Rev. C **104**, 044613 (2021).
 - [27] H. Gil, C. H. Hyun and K. S. Kim, Inclusive electron scattering in the quasielastic region with the Korea-IBS-Daegu-SKKU density functional, Phys. Rev. C **105**, 024607 (2022).
 - [28] K. S. Kim, H. Gil and C. H. Hyun, Quasielastic charged-current neutrino-nucleus scattering with nonrelativistic nuclear energy density functionals, Phys. Lett. B **833**, 137273 (2022).
 - [29] P. T. P. Hutaurok, H. Gil, S.-i. Nam and C. H. Hyun, Effect of nucleon effective mass and symmetry energy on the neutrino mean free path in a neutron star, Phys. Rev. C **106**, 035802 (2022).
 - [30] H. Gil, C. H. Hyun and K.S. Kim, Neutron skin of ^{27}Al with Skyrme and Korea-IBS-Daegu-SKKU density functionals, Mod. Phys. Lett. A **39**, 2350184 (2024).
 - [31] P. T. P. Hutaurok, H. Gil, S.-i. Nam and C. H. Hyun, Effects of symmetry energy on the equation of state for hybrid neutron stars, J.Korean Phys.Soc. **85**, 617 (2024).
 - [32] D. Sen, H. Gil and C. H. Hyun, Hadron-quark phase transition in the neutron star with vector MIT bag model and Korea-IBS-Daegu-SKKU functional, Front. Astron. Space Sci. **11**, 1421839 (2024).
 - [33] A. Guha, D. Sen and C. H. Hyun, Non-radial oscillations of hadronic neutron stars, quark stars, and hybrid stars: calculation of f , p , and g mode frequencies, Eur. Phys. J. C **85**, 442 (2025).
 - [34] H. Togashi, D. Sen, H. Gil and C. H. Hyun, Influence of the Effective Mass on the Properties of Nuclear Matter at Finite Density and Temperature, Symmetry **17**, 445 (2025).

- [35] A. Guha, D. Sen, H. Gil, H. Togashi and C. H. Hyun, f and p mode oscillation of proto-neutron stars with systematic variation of the nucleon effective mass, e-Print: 2508.07000 [nucl-th].
- [36] S.-I. Ando, Elastic α - ^{12}C scattering at low energies in cluster effective field theory, Eur. Phys. J. A **52**, 130 (2016).
- [37] S.-I. Ando, Elastic α - ^{12}C scattering at low energies with the bound states of ^{16}O in effective field theory, Phys. Rev. C **97**, 014604 (2018).
- [38] S.-I. Ando, Elastic α - ^{12}C scattering at low energies with the sharp resonant 0_3^+ state of ^{16}O , Phys. Rev. C **102**, 034611 (2020).
- [39] S.-I. Ando, Elastic α - ^{12}C scattering at low energies with the resonant 2_2^+ and 2_3^+ states of ^{16}O , Phys. Rev. C **105**, 064603 (2022).
- [40] S.-I. Ando, S matrices of elastic α - ^{12}C scattering at low energies in effective field theory, Phys. Rev. C **107**, 045808 (2023).
- [41] X. D. Tang *et al.*, Determination of the $E1$ component of the low-energy $^{12}\text{C}(\alpha, \gamma)^{16}\text{O}$ cross section, Phys. Rev. C **81**, 045809 (2010).
- [42] N. Oulebsir *et al.*, Indirect study of the $^{12}\text{C}(\alpha, \gamma)^{16}\text{O}$ reaction via the $^{12}\text{C}(^7\text{Li}, t)^{16}\text{O}$ transfer reaction, Phys. Rev. C **85**, 035804 (2012).
- [43] P. Tischhauser *et al.*, Measurement of elastic $^{12}\text{C} + \alpha$ scattering: Details of the experiment, analysis, and discussion of phase shifts, Phys. Rev. C **79**, 055803 (2009).
- [44] R. J. Deboer *et al.*, The $^{12}\text{C}(\alpha, \gamma)^{16}\text{O}$ reaction and its implications for stellar helium burning Rev. Mod. Phys. **89**, 035007 (2017).
- [45] R. Plaga, H. W. Becker, A. Redder, C. Rolfs, H. P. Trautvetter, and K. Langanke, The scattering of alpha particles from ^{12}C and the $^{12}\text{C}(\alpha, \gamma)^{16}\text{O}$ stellar reaction rate, Nucl. Phys. A **465**, 291-316 (1987).
- [46] Z. R. Iwinski, L. Rosenberg, and L. Spruch, Radiative capture estimates via analytic continuation of elastic-scattering data, and the solar-neutrino problem, Phys. Rev. C **29**, 349(R) (1984).
- [47] S.-I. Ando, Elastic α - ^{12}C scattering with the ground state of ^{16}O at low energies in effective field theory, J. Korean Phys. Soc. **73**, 1452 (2018).
- [48] S.-I. Ando, Fixing effective range parameters in elastic α - ^{12}C scattering: an impact on resonance 2_4^+ state of ^{16}O and S_{E2} factor of $^{12}\text{C}(\alpha, \gamma)^{16}\text{O}$, Chinese Phys. C **49**, 094107 (2025).
- [49] P. Virtanen *et al.*, SciPy 1.0: Fundamental algorithms for scientific computing in Python,

- Nat. Methods **17**, 261 (2020).
- [50] R. Storn and K. Price, Differential evolution – A simple and efficient heuristic for global optimization over continuous spaces, J. Global Optim. **11**, 341 (1997).
- [51] K. V. Price, R. M. Storn, and J. A. Lampinen, *Differential Evolution: A Practical Approach to Global Optimization* (Springer, Berlin, 2005).
- [52] D. Foreman-Mackey, D. W. Hogg, D. Lang, J. Goodman, emcee: The MCMC Hammer, Publ. Astron. Soc. Pac. **125**, 306 (2013).
- [53] D. R. Tilley, H. R. Weller and C. M. Cheves, Energy levels of light nuclei $A = 16$, Nucl. Phys. A **564**, 1 (1993).
- [54] S.-I. Ando, ANCs of the bound states of ^{16}O deduced from elastic α - ^{12}C scattering data, Few-Body Syst. **65**, 7 (2024).
- [55] See a textbook, e.g., C. Iliadis, Nuclear Physics of Stars, Wiley-VCH Verlag GmbH & Co. KGaA (2007).
- [56] S.-I. Ando, Radiative decay of the subthreshold 1_1^- and 2_1^+ states of ^{16}O in cluster effective field theory, Phys. Rev. C **109**, 015801 (2024).
- [57] S.-I. Ando, Retraction: Radiative decay of the subthreshold 1_1^- and 2_1^+ states of ^{16}O in cluster effective field theory [Phys. Rev. C **109**, 015801 (2025)], Phys. Rev. C **112**, 049902 (2025).

Appendix A: Relations between the laboratory frame and center-of-mass frame

Transformation of the differential cross section and scattering angle between the laboratory frame and the center-of-mass frame is well known [55]. We present only the formulas necessary in the present work: we need two relations of the scattering angles and the differential cross sections in the non-relativistic limit, i.e., we ignored the $1/m$ corrections. (The α energy, E_α , in the laboratory frame is related to the energy, E , of the α - ^{12}C system in the center-of-mass frame as $E_\alpha = \frac{4}{3}E$.)

Using the γ factor, $\gamma = m_\alpha/m_C = 1/3$, the relation of the scattering angles reads

$$\cos \theta = -\frac{1}{3} \sin^2 \theta_L \pm \frac{1}{3} \sqrt{(1 - \sin^2 \theta_L)(9 - \sin^2 \theta_L)}, \quad (18)$$

where θ and θ_L are the scattering angles in the center-of-mass frame and the laboratory

frame, respectively. The relation for the differential cross sections reads

$$\sigma_L(\theta_L) = \sigma(\theta) \frac{d(\cos \theta_L)}{d(\cos \theta)}, \quad (19)$$

where σ_L is the differential cross section in the laboratory frame and

$$\frac{d(\cos \theta_L)}{d(\cos \theta)} = \frac{1 + \frac{1}{3} \cos \theta}{\left(\frac{10}{9} + \frac{2}{3} \cos \theta\right)^{3/2}}. \quad (20)$$

Appendix B: Fixing the effective range parameters, r_0 and r_2

In this appendix, we review the methods to fix the effective range parameters, r_0 and r_2 , by using the binding energy of the ground 0_1^+ state of ^{16}O and a value of the ANC of 2_1^+ state of ^{16}O . To fix r_0 , we adopt two conditions on the inverse of the ^{16}O propagator for $l = 0$; one is $D_0(i\gamma_{01}) = 0$ and the other is $D_0(i\gamma_{02}) = 0$, where γ_{01} and γ_{02} are the binding momenta for the 0_1^+ and 0_2^+ states of ^{16}O , respectively, $\gamma_{01} = \sqrt{2\mu B_{01}}$ and $\gamma_{02} = \sqrt{2\mu B_{02}}$. B_{01} and B_{02} are the binding energies of 0_1^+ and 0_2^+ states of ^{16}O with respect to the α - ^{12}C state. By using the two conditions mentioned above, one has [56, 57]

$$\begin{aligned} D_0(p) = & -\frac{1}{4} [\gamma_{01}^2 \gamma_{02}^2 + (\gamma_{01}^2 + \gamma_{02}^2) p^2 + p^4] P_0 \\ & + [-\gamma_{01}^4 \gamma_{02}^2 - \gamma_{01}^2 \gamma_{02}^4 - (\gamma_{01}^4 + \gamma_{01}^2 \gamma_{02}^2 + \gamma_{02}^4) p^2 + p^6] Q_0 \\ & - 2\kappa \left[\frac{\gamma_{02}^2 + p^2}{\gamma_{01}^2 - \gamma_{02}^2} H_0(i\gamma_{01}) - \frac{\gamma_{01}^2 + p^2}{\gamma_{01}^2 - \gamma_{02}^2} H_0(i\gamma_{02}) + H_0(p) \right]. \end{aligned} \quad (21)$$

To fix r_2 , one may use Eq. (12). Thus, one has

$$\begin{aligned} r_2 = & -\frac{1}{2} \gamma_2^4 \left[\frac{\Gamma(3 + \kappa/\gamma_2)}{|C_b|_2} \right]^2 + \frac{1}{12} \kappa^3 \\ & - \left(P_2 + \frac{17}{20} \kappa \right) \gamma_2^2 - 6 \left(Q_2 - \frac{757}{4032\kappa} \right) \gamma_2^4 - \frac{289}{1260\kappa^3} \gamma_2^6 + \frac{2455}{11088\kappa^5} \gamma_2^8. \end{aligned} \quad (22)$$

Appendix C: Effective range parameters

TABLE IV: Fitted parameters for $l = 0$ and $l = 1$. Three values are presented for each parameter. The values in the first row are obtained from fits to the phase-shift data, while those in the second and third rows are determined by fitting the differential cross-section data using the DE method and MCMC analysis, respectively. Parameters marked with an asterisk (*) are fixed by other experimental data, and blank entries indicate that the corresponding parameters are not included in the fit.

l_{π}^{π}	p^0	p^2	p^4	p^6
$0_1^+, 0_2^+$	a_0 (fm)	r_0 (fm)	P_0 (fm ³)	Q_0 (fm ⁵)
Phase shift	*	*	-0.03452(2)	0.001723(7)
DE	*	*	-0.034365	0.001677
MCMC	*	*	-0.034423(58)	0.001688(20)
0_3^+	$E_{R(03)}$ (MeV)	$\Gamma_{R(03)}$ (keV)		
	4.8883(1)	1.35(3)		
	4.892853	0.917		
	4.892851(15)	0.891(11)		
0_4^+	$E_{R(04)}$ (MeV)	$\Gamma_{R(04)}$	$a_{(04)}$ (MeV ⁻¹)	$b_{(04)}$ (MeV ⁻²)
	*	*	0.756(7)	0.167(4)
	*	*	0.843	0.217
	*	*	$0.815^{+0.017}_{-0.010}$	$0.195^{+0.009}_{-0.008}$
$1_1^-, 1_2^-$	a_1 (fm ³)	r_1 (fm)	P_1 (fm ⁻¹)	Q_1 (fm ⁻³)
	*	0.415314(7)	-0.57428(7)	0.02032(2)
	*	0.415386	-0.57383	0.02038
	*	0.415342(12)	-0.57430(12)	0.02023(4)
1_3^-	$E_{R(13)}$ (MeV)	$\Gamma_{R(13)}$ (keV)	$a_{(13)}$ (MeV ⁻¹)	$b_{(13)}$ (MeV ⁻²)
	*	*	0.43(25)	3.8(7)
	*	*	0.22	7.6
	*	*	$0.28^{+0.10}_{-0.11}$	7.7(5)

TABLE V: Fitted parameters for $l = 2$ and $l = 3$. See the caption of Table IV for detailed descriptions.

l_{ith}^π	p^0	p^2	p^4	p^6	p^8
2_1^+	a_2 (fm ³)	r_2 (fm ⁻³)	P_2 (fm ⁻¹)	Q_2 (fm)	
	*	*	-1.049(2)	0.141(2)	
	*	*	-1.054	0.130	
	*	*	-1.092(2)	0.111(1)	
2_2^+	$E_{R(22)}$ (MeV)	$\Gamma_{R(22)}$ (keV)			
	2.68308(1)	0.76(1)			
	2.61925	0.73			
	$2.61191^{+0.00227}_{-0.00207}$	0.19(6)			
2_3^+	$E_{R(23)}$ (MeV)	$\Gamma_{R(23)}$ (keV)	$a_{(23)}$ (MeV ⁻¹)	$b_{(23)}$ (keV)	
	4.3536(1)	74.5(1)	1.2(1)	0.6(1)	
	4.35897	79.3	1.19	1.50	
	4.35902(6)	79.1(1)	0.96(4)	1.17(5)	
2_4^+	$E_{R(24)}$ (MeV)	$\Gamma_{R(24)}$ (keV)	$a_{(24)}$	$b_{(24)}$	
	5.89(2)	237(19)	0.67(9)	0.2(1)	
	*	*			
	*	*			
$3_1^-, 3_2^-$	a_3 (fm ⁷)	r_3 (fm ⁻⁵)	P_3 (fm ⁻³)	Q_3 (fm ⁻¹)	R_3 (fm)
	*	0.0355(2)	-0.446(9)	0.311(5)	-0.152(3)
	*	0.0343	-0.436	0.313	-0.152
	*	0.0361(3)	-0.389(8)	0.336(4)	-0.138(2)
3_3^-	$E_{R(33)}$ (MeV)	$\Gamma_{R(33)}$ (keV)	$a_{(33)}$ (MeV ⁻¹)	$b_{(33)}$ (MeV ⁻²)	
	*	*	32(32)	$3.2(32) \times 10^2$	
	*	*			
	*	*			

TABLE VI: Fitted parameters for $l = 4$, $l = 5$, and $l = 6$. See the caption of Table IV for detailed descriptions.

l_{ith}^π	p^0	p^2	p^4	p^6
4_1^+	$E_{R(41)}$ (MeV)	$\Gamma_{R(41)}$ (keV)	$a_{(41)}$ (MeV $^{-1}$)	$b_{(41)}$ (MeV $^{-2}$)
	3.19606(1)	25.91(1)	0.740(3)	0.304(5)
	3.19878	27.71	0.741	0.608
	3.19875(2)	27.67(6)	0.387(34)	1.028(37)
4_2^+	$E_{R(42)}$ (MeV)	$\Gamma_{R(42)}$ (keV)		
	3.93655(2)	0.425(4)		
	4.29785	0.340		
	4.29617(123)	0.147(28)		
4_3^+	$E_{R(43)}$ (MeV)	$\Gamma_{R(43)}$ (keV)	$a_{(43)}$ (MeV $^{-1}$)	$b_{(43)}$ (MeV $^{-2}$)
	*	*	0.889(6)	0.216(3)
	*	*	0.421	0.039
	*	*	0.411(5)	0.036(1)
5_1^-	$E_{R(51)}$ (MeV)	$\Gamma_{R(51)}$ (keV)	$a_{(51)}$ (MeV $^{-1}$)	$b_{(51)}$ (MeV $^{-2}$)
	*	*	0.572(6)	0.104(2)
	*	*	0.602	0.114
	*	*	0.580(12)	0.102(4)
(bg)		r_6 (fm $^{-11}$)	P_6 (fm $^{-9}$)	
		-0.3(2)	2(1)	
		-0.20	0.22	
		$-0.24^{+0.35}_{-0.38}$	$1.96^{+1.48}_{-1.10}$	
6_1^+	$E_{R(61)}$ (MeV)	$\Gamma_{R(61)}$ (keV)	$a_{(61)}$ (MeV $^{-1}$)	$b_{(61)}$ (MeV $^{-2}$)
	*	*	0.8(1)	0.18(4)
	*	*	0.723	0.134
	*	*	$0.751^{+0.029}_{-0.024}$	$0.146^{+0.029}_{-0.024}$